

# Intracellular Nanomaterial Delivery *via* Spiral Hydroporation

GeoumYoung Kang, Daniel W. Carlson, Tae Ho Kang, Seungki Lee, Simon J. Haward, Inhee Choi, Amy Q. Shen, and Aram J. Chung\*

Cite This: *ACS Nano* 2020, 14, 3048–3058

Read Online

ACCESS |

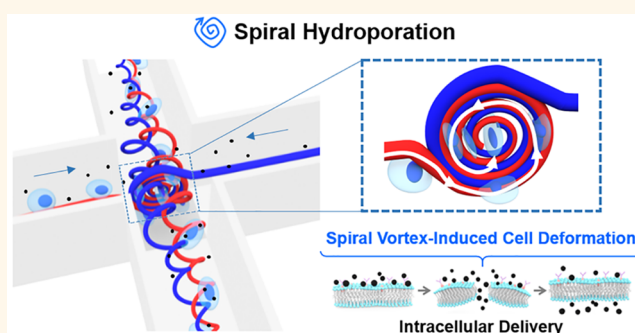
Metrics & More

Article Recommendations

Supporting Information

**ABSTRACT:** In recent nanobiotechnology developments, a wide variety of functional nanomaterials and engineered biomolecules have been created, and these have numerous applications in cell biology. For these nanomaterials to fulfill their promises completely, they must be able to reach their biological targets at the subcellular level and with a high level of specificity. Traditionally, either nanocarrier- or membrane disruption-based method has been used to deliver nanomaterials inside cells; however, these methods are suboptimal due to their toxicity, inconsistent delivery, and low throughput, and they are also labor intensive and time-consuming, highlighting the need for development of a next-generation, intracellular delivery system. This study reports on the development of an intracellular nanomaterial delivery platform, based on unexpected cell-deformation phenomena *via* spiral vortex and vortex breakdown exerted in the cross- and T-junctions at moderate Reynolds numbers. These vortex-induced cell deformation and sequential restoration processes open cell membranes transiently, allowing effective and robust intracellular delivery of nanomaterials in a single step without the aid of carriers or external apparatus. By using the platform described here (termed spiral hydroporator), we demonstrate the delivery of different nanomaterials, including gold nanoparticles (200 nm diameter), functional mesoporous silica nanoparticles (150 nm diameter), dextran (hydrodynamic diameters between 2–55 nm), and mRNA, into different cell types. We demonstrate here that the system is highly efficient (up to 96.5%) with high throughput (up to  $1 \times 10^6$  cells/min) and rapid delivery ( $\sim 1$  min) while maintaining high levels of cell viability (up to 94%).

**KEYWORDS:** intracellular delivery, nanoparticle delivery, macromolecule delivery, cell transfection, hydroporator, hydroporation, inertial microfluidics



Nanomaterials such as functional nanoparticles and synthetic biomolecules have attracted considerable attention, particularly from the cell biology community.<sup>1–6</sup> For instance, gold nanoparticles (GNPs) can be synthesized with specific shapes and configurations and can be conjugated with other materials for drug delivery, imaging, single-molecule, or subcellular organelle tracking, biosensing, and diagnosis.<sup>1–3</sup> As another example, genetic nanomaterials such as DNAs, RNAs, or RNA/DNA nanovehicles<sup>4</sup> can be synthesized and introduced into cells for cell-based therapy, gene editing, and cell reprogramming.<sup>5,6</sup> To achieve the desired functions, nanomaterials must pass through the lipid bilayer cell membrane that separates the cell interior from the environment. Because cell membranes selectively and actively control the entry of substances into cells, using membrane transport protein channels (known as endocytosis),<sup>7</sup> only small molecules, particles, and ions can easily diffuse or pass through them. Thus, for larger nanomaterials, effective uptake *via*

endocytosis is difficult to achieve without complex nanomaterial chemical surface modification.

To facilitate the nanomaterial endocytic process, numerous synthetic nanocarriers such as lipids, polymers, inorganic nanomaterials, cell-penetrating peptides (CPPs), and other targeting or stabilizing agents have been developed.<sup>8</sup> These nanocarriers can cross the cell membrane because they take advantage of natural endocytic pathways based on their cell membrane interactions and physicochemical properties. However, nanomaterials often reside in liposomal vesicles without being exposed to the intracellular environment (*i.e.*, endosomal entrapment), which leads to the degradation of

**Received:** October 8, 2019

**Accepted:** February 12, 2020

**Published:** February 18, 2020

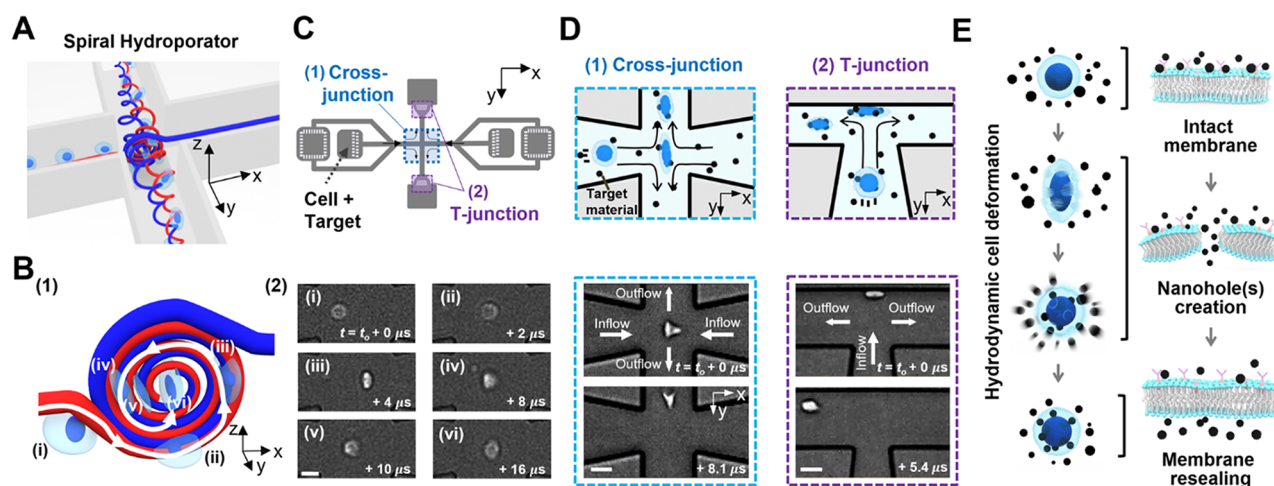


**Figure 1.** Spiral hydroporation for intracellular nanomaterial delivery. (A) Schematic depicting spiral flow motion at a cross-junction channel. (B) (1) Illustration of spiral vortex-induced cell deformation and (2) high-speed microscope images showing rotational cell motions (scale bar: 10  $\mu\text{m}$ ). (C) CAD layout of the hydroporation microfluidic device, consisting of (1) a cross-junction and (2) two dividing T-junction channels. (D) Hydrodynamic cell deformation *via* (1) the spiral vortex at the cross-junction and (2) cell-wall collision at the T-junction(s) (scale bars: 20 and 30  $\mu\text{m}$  for (1) and (2), respectively). (E) Schematic illustrating nanomaterial delivery into cell cytosols.

lysosomes or regurgitation back to the cell surface.<sup>9</sup> For nucleic acid delivery, viral carriers (*e.g.*, vectors such as lentivirus, retrovirus, and adenovirus) are highly preferred to transfect cells owing to their high specificity. However, the safety, cost, and complexity of their preparation are critical concerns,<sup>10</sup> indicating that true, accurate, safe, and cost-effective internalization of nanomaterials remains a long-standing challenge.

Alternatively, an entry point on the cell membrane can be created by applying external physical forces. For instance, the cell membrane can be opened by microinjection, using a sharp glass micropipette to insert nanomaterials into the cells. Electroporation is another entry mechanism example, and in this method, discontinuities are created in cell and nuclear membranes by applying a high voltage. These membrane disruption-based techniques permit target nanomaterial- and cell-type-insensitive delivery; however, excessive cell damage, inconsistent delivery, and low scalability are unavoidable drawbacks.

To address this open challenge, micro- and nanotechnologies have been investigated, leading to a wide variety of solutions.<sup>11–19</sup> Among these, microfluidics have exhibited high potential because of their precise fluidic controls and cell manipulation with high spatiotemporal resolution.<sup>20</sup> Most state-of-the-art, microfluidic delivery platforms mechanically deform cells without external forces, using mechanisms involving electrical or acoustic forces, for example, to create transient discontinuities in the cell membrane either by passing cells through narrow channel structures such as bottlenecks/ridges<sup>21–24</sup> or poking cells.<sup>25,26</sup> These microfluidic approaches have high promises for the delivery of various nanomaterials; however, their designs are susceptible to clogging, which is a nontrivial issue, substantially lowering their practicality.

Recently, Kizer *et al.*,<sup>27</sup> reported a microfluidic, clogging-free, nanomaterial intracellular delivery platform that hydrodynamically deforms cells in a cross-junction, producing transient nanopores in the cell membrane. The platform successfully delivered a varied selection of molecules; however, the delivery of larger nanomaterials (>50 nm) was limited owing to a lack of knowledge about the fluid–cell interactions. It must be mentioned that there is a predominant

misconception in the microfluidics field that “symmetric and uniform planar extensional flow” arises in a cross-junction channel at moderate Reynolds numbers ( $Re$ ; a dimensionless parameter describing the ratio of inertial force to viscous force), resulting in symmetric cell elongation.<sup>28</sup> In fact, this is only true at low  $Re$  flows.<sup>29</sup>

In this study, we introduce an unexpected cell deformation phenomenon that leverages the spiral vortex and vortex breakdown in a cross-junction at moderate  $Re$ , leading to highly effective intracellular delivery of large nanomaterials. Briefly, in this method, cells in the spiral vortex flow undergo an intrinsic hydrodynamic cell deformation–restoration process (we subsequently refer to this mechanism as “spiral hydroporation”), which opens the cell membrane, allowing rapid transport of exogenous nanomaterials into the cytosol. Based on this spiral hydroporation platform, we have achieved the highly efficient (up to 96.5%), high-throughput (up to  $1 \times 10^6$  cells/min), rapid ( $\sim 1$  min) delivery of different large nanoparticles (200 nm gold and 150 nm mesoporous silica nanoparticles) and macromolecules (>2000 kDa dextran and 996 nt mRNA) into cells while maintaining high cell viability (up to 94%).

## RESULTS AND DISCUSSION

**Design and Operating Principles.** The presented spiral hydroporation platform (Figure 1C) comprises a cross-junction and two dividing T-junction channels. The cell suspension, with target nanomaterials mixed in, is pumped into two opposing channels at different flow rates ( $Re \approx 0$ –366) and exits through two opposing outlet T-junction channels. We found that at moderate  $Re$ , instead of symmetric cell elongation,<sup>28</sup> the cells spiral down, exhibiting large deformation as they approach the stagnation point (see Figure 1B and Movies S1 and S2). With respect to the cross-junction geometry, it has been reported that such intersecting flows are prone to instability,<sup>30</sup> and we postulated that flow instability near the stagnation point induces a strong spiral vortex, accounting for the observed cell deformation phenomenon. The observed spiral flow motion/pattern agrees very well with that reported by Haward *et al.*<sup>31,32</sup> who

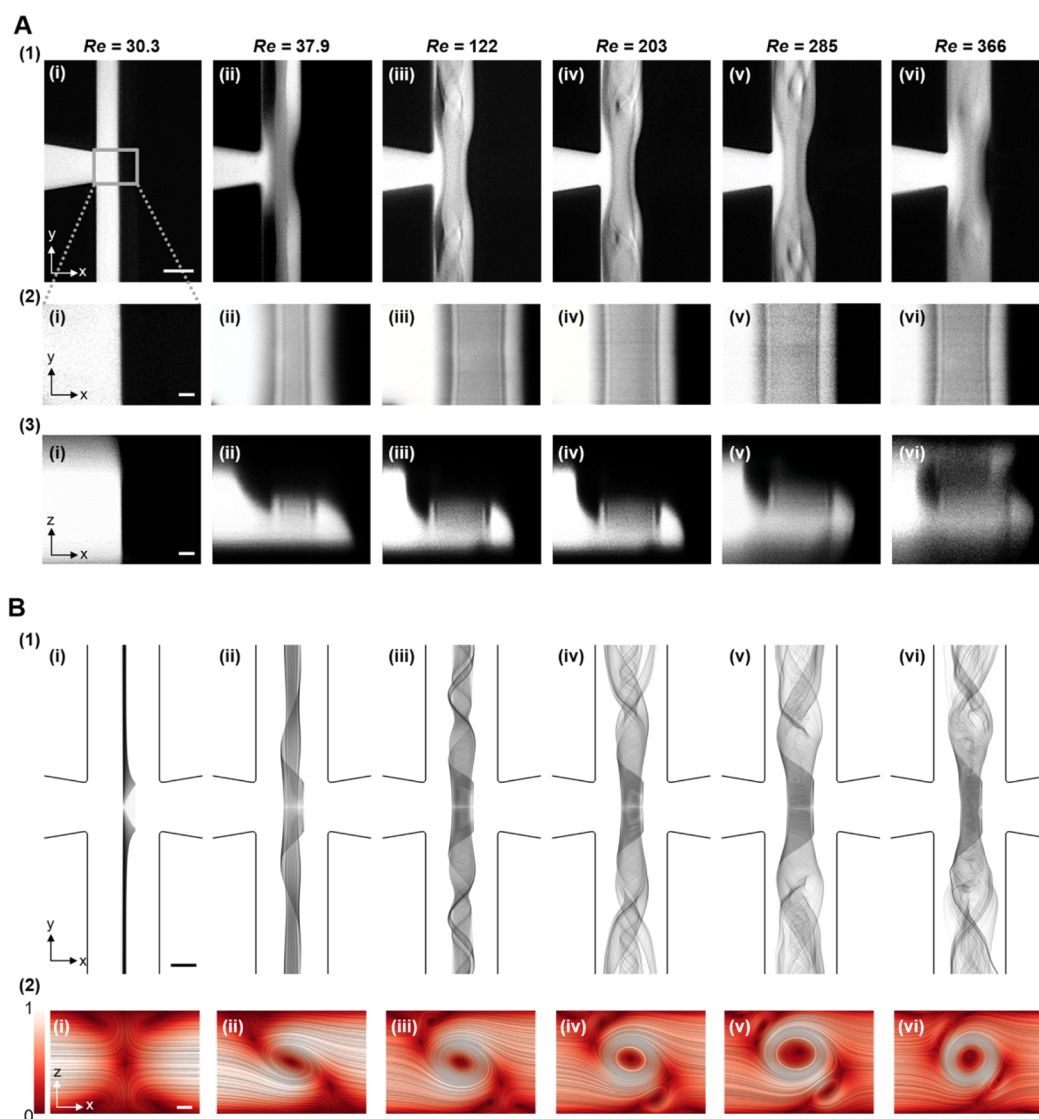


**Figure 2.** Experimental and numerical flow characterization. (A) (1) Fluorescence and (2–3) confocal microscope images of the steady flow regimes at the cross-junction, at different  $Re$ . Onset of steady engulfment flow at  $Re_c = 37.9$ , and higher complex flow patterns beyond  $Re_c$  (scale bars: 40 and 6  $\mu\text{m}$ , for (1) and (2–3), respectively). (B) (1) Simulated streamlines and (2) midplane contours of the normalized velocity at different  $Re$  (white and black legend indicating normalized velocities of 1 and 0, respectively). Steady flow at  $Re = 30.3$ –122, and a periodic oscillation of the central vortex at  $Re = 203$ –366 can be seen (scale bars representing 20 and 6  $\mu\text{m}$ , for (1) and (2), respectively).

examined the spiral vortex flow (without particles or cells) in mm-sized, cross-junction devices; for more details, refer to the section below, in which we experimentally measure and numerically predict vorticity at the micrometer scale.

As the cells leave the stagnation point region, they are guided to the channel center by inertia<sup>33–35</sup> and collide with one of the T-junction channel walls,<sup>36</sup> resulting in additional cell deformation (see Figure 1D (2) and Movie S3). We hypothesize that this repeated cell deformation–restoration process generates more nanoholes in the cell membranes, enabling enhanced convective and diffusive transport of the target materials into the cytosol (see Figure 4 for details). Note that the nanoholes created in the cell membrane (Figure 1E) are resealed *via* a self-repairing mechanism within 1 min,<sup>10</sup> and even this time can be adjusted by modulating the solution's calcium concentration.<sup>37</sup>

**Spiral Flow Characterization.** For detailed investigation of the spiral cell deformation phenomenon, we microscopically investigated spiral vortex formation in a cross-junction channel

both experimentally and numerically. For flow visualization (see Materials and Methods section for details), all experiments were performed at room temperature, over a range of  $Re$  ( $Re = \rho U D_h / \mu$ , where  $\rho$  is the fluid density,  $U$  is the average flow velocity,  $D_h$  is the hydraulic diameter, and  $\mu$  is the dynamic viscosity of the carrier fluid). Deionized water (DI) was injected at both the left and right inlets, with fluorescent dye added to the water injected on the left (see Materials and Methods). Fluorescent images of the XY plane (top view), which capture evolution of the vortex as a function of  $Re$ , can be seen in Figure 2A (1). At the lowest Reynolds number, the interface between the two fluid streams remains sharp and symmetric, while three-dimensional, swirling motions start to become apparent at a Reynolds number of 37.9 (defined as the critical Reynolds number,  $Re_c$ ); the crossover becomes stronger and more complex as  $Re$  increases. Note that this swirling flow motion is completely different from what was widely believed to be a symmetric planar extensional flow in cross-junction channels, based on previous reports.<sup>27,28,38,39</sup>

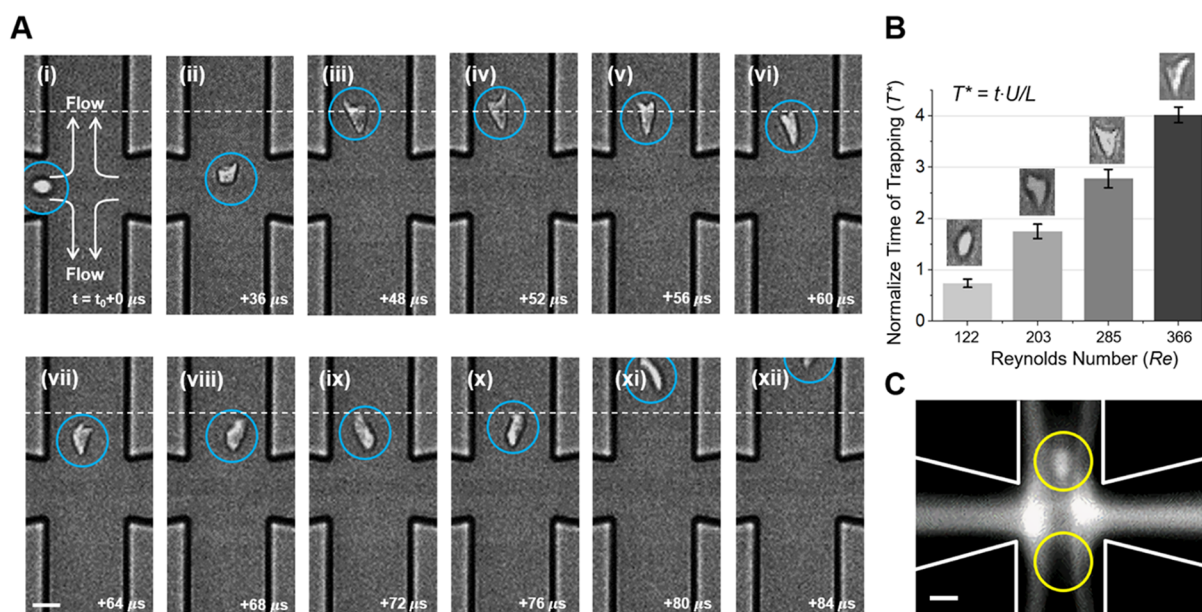


**Figure 3.** Vortex breakdown-induced cell trapping and deformation. (A) High-speed microscopic images showing MDA-MB-231 cell trapping behavior caused by vortex breakdown ( $Re = 285$ ). (B) Normalized time of trapping as a function of  $Re$ . (Insets) Representative cell deformation images for corresponding  $Re$  (error bars: mean  $\pm$  1 SD,  $N = 3$ ). (C) Image showing a rigid,  $4.8 \mu\text{m}$  fluorescent bead becoming trapped, at  $Re = 203$ , due to vortex breakdown. The yellow circles indicate the two trapping regions caused by channel symmetry (all scale bars:  $20 \mu\text{m}$ ).

To examine the interface between the fluid streams near the crossover region in more detail, a confocal microscope (FV1000, Olympus, Tokyo, Japan) was employed. It can be seen in Figure 2A (2–3), that, with the further increase in  $Re$ , an anticlockwise spiral vortex developed beyond  $Re_c$ , and the spiral expanded both vertically and horizontally. The vortex pattern and  $Re_c$  onset for the crossover agree very well with previous studies, in which the spiral vortex was measured at the mm scale.<sup>31,40,41</sup>

To gain deeper insights, we also performed numerical analysis, using OpenFOAM<sup>42</sup> (see Materials and Methods for numerical computation details). Each experimental cross-junction case (Figure 2A) was solved as an incompressible fluid, and analyzed with respect to the presence of both steady-state and transient flows. In addition, near  $Re_c$ , the flow increased with a step size of  $Re = 2$ , and transitioned into a central vortex at  $Re = 36$ , which was in agreement with the experiments. Minor discrepancies can be attributed to geometrical differences in the polydimethylsiloxane (PDMS) deformation (bulging) and to fabrication imperfections.

The fluid solver reaches a tightly converged (velocity and pressure residuals below  $10^{-7}$ ), steady-state solution, at  $Re = 30.3, 37.9$ , and  $122$  (Movie S4). At  $Re = 203$ , the steady-state residual tolerance is not met; thus, a transient incompressible solver was applied. Compared with the solution at  $Re = 122$ , where the vortex core was static, the vortex at  $Re = 203$  oscillates perpendicular to the inlets, primarily in the direction of the Z-axis (Figure 2B (2) (iv), and Movie S5). At higher flow rates and  $Re = 285$  and  $366$ , the oscillation of the core vortex becomes more elliptical in the XZ plane, and pulse-like, with the vortex periodically encountering the walls of the channel and breaking apart before reforming (Movie S6), all of which explains the cells' intrinsic deformation behaviors at different  $Re$ , as observed in our experiments.

**Vortex Breakdown-Induced Cell Trapping and Deformation.** The spiral hydroporator is designed to open cell

membranes by rapidly deforming cells *via* spiral vortex and cell wall collisions in a sequential manner (Figure 1). After passing the first spiral cell deformation region, unexpected cell trapping phenomena were observed (Movie S7). As was strikingly shown in Figure 3A, slightly above the stagnation point, a cell travels up and down repeatedly, for approximately  $30 \mu\text{s}$ , and then migrates toward the outlet. To quantify the strength of this cell-trapping dependency on  $Re$ , we defined the normalized time of trapping ( $T^* = tU/L$ , where  $t$  is the time necessary for the cell to escape the trapping region,  $U$  is the average fluid velocity, and  $L$  is the trapping region length; see Figure S1 for the geometric configuration). Normalized time is introduced here to avoid the misconception that a faster flow rate corresponds to a shorter cell trapping time (*i.e.*, less cell deformation), which is not the case in our study. As presented in Figure 3B, the normalized time for trapping and cell deformation increased with increasing  $Re$ , and this extra cell perturbation is considered to enhance nanoparticle delivery (details are provided in the section below).

Our observation agrees well with recent work by Vigolo *et al.*,<sup>43</sup> who reported bubble trapping at the T-junction, and Chan *et al.*,<sup>44</sup> who discussed low-density particle trapping at the T-junction. Those trapping incidents were felt to have been based on recirculating flow, also known as vortex breakdown, which often develops when the vorticity decay is presented by swirling flows.<sup>45</sup> On the vortex axis, pressure gradients are generated in the opposite direction of the outlet flows, toward the center of the cross,<sup>30</sup> allowing cells to travel against the flow (Figure 3A), appearing to be trapped. In previous studies,<sup>43,44</sup> bubbles or low-density particles compared with the carrier fluid (water) were used, but here we report that cells and rigid spheres (Figure 3C), with density values similar or slightly higher to that of the carrier fluid, can also be trapped. Note that rigid polystyrene beads could not be trapped as efficiently as cells (data not shown), possibly due to a shape-

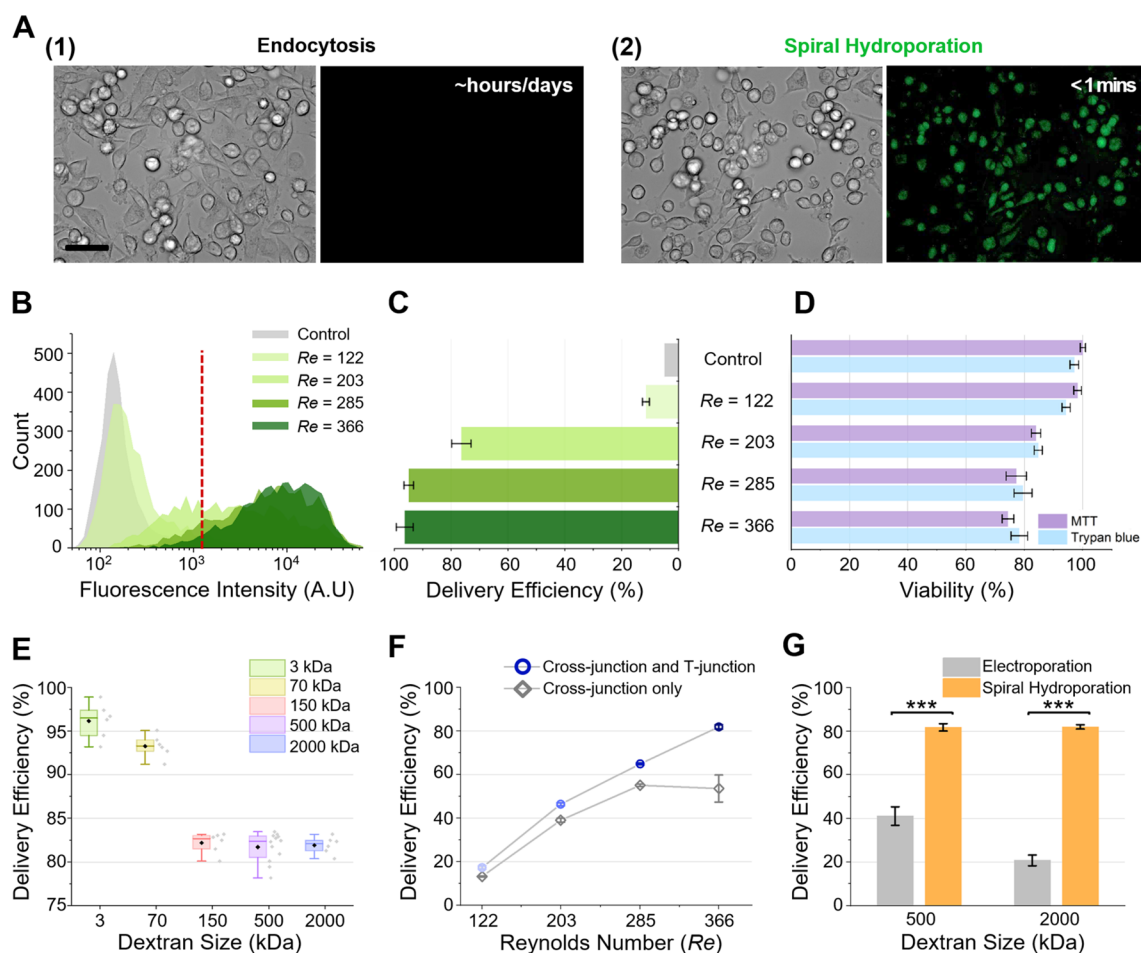


**Figure 4.** Characterization of intracellular dextran delivery. (A) Bright-field and fluorescent images showing delivery of 3–5 kDa FITC-dextran into MDA-MB-231 cells *via* (1) endocytosis (control) and (2) spiral hydroporation, after 18 h (scale bar: 40  $\mu\text{m}$ ). (B) Fluorescence intensity histograms at different  $Re$ . (C) Delivery efficiency and (D) cell viability as a function of  $Re$ . (E) Dependence of delivery efficiency on different dextran sizes. (F) Delivery efficiency for 2000 kDa FITC-dextran in the cases of a cross-junction and a combination of cross- and T-junctions. (G) Comparisons of delivery efficiency by either electroporation or spiral hydroporation, for 500 and 2000 kDa FITC-dextran. All error bars except (E) indicate the mean  $\pm 1$  SD ( $N = 3$ ), and \*\*\* represents a  $P$ -value below 0.001. The error bars in (E) represent maximum and minimum boundaries, with the straight lines in the box showing the median, and the diamond markers indicating the mean ( $N = 6$ ).

dependent drag<sup>46</sup> that was associated with the centrifugal force.

#### Characterization of Intracellular Dextran Delivery.

The spiral hydroporation process allows target nanomaterials to be transported through the created nanoholes on the cell membrane, yielding highly efficient intracellular delivery. To characterize spiral hydroporation delivery performance, we first tested delivery of 3–5 kDa fluorescein isothiocyanate (FITC)-conjugated dextran into MDA-MB-231 cells. We chose MDA-MB-231 as our delivery vehicle because it is reportedly one of the more difficult cell lines for dextran delivery.<sup>27</sup> Details can be found in the **Materials and Methods** section, but briefly, we injected the mixture of cells and nanomaterials into the spiral hydroporation, collected and washed them, and imaged the cells after 18 h. As presented in **Figure 4A**, strong FITC signals were detected for cells treated with the spiral hydroporation, and not for the endocytosis control group.

To assess the delivery amount, we measured the fluorescence signal intensity of each cell, using a flow cytometer (see **Materials and Methods** section). As previously reported,<sup>21</sup> we defined the delivery efficiency as the fraction of the fluorescence signals above 5% (red dotted line in **Figure**

**4B**) after delivery, which was set as the endocytosis control (gray shading in **Figure 4B**), accounting for the endocytosis, autofluorescence, and surface binding of the FITC-dextran. As shown in **Figure 4B,C**, at  $Re = 366$ , approximately 96.5% delivery efficiency was achieved, and as the  $Re$  increased, the fluorescence intensity increased, causing the histogram profile to shift to the right, which implies that we can control the delivery amount by adjusting the  $Re$  deterministically. Note that the level of delivery must be understood from the mean fluorescence intensity (MFI) values as well and has been plotted in **Figure S2**.

We also characterized the dependency of delivery efficiency on the sample (cell) concentration and observed that delivery efficiency started to decrease if the sample concentration became higher than  $4 \times 10^6$  cells/mL (**Figure S3**). Thus, at  $Re = 366$ , with a sample concentration of approximately  $2 \times 10^6$  cells/mL, a total throughput of  $1 \times 10^6$  cells/min was achieved. It must be emphasized that the entire delivery process takes approximately 1 min, representing rapid intracellular nanomaterial delivery.

With respect to cell viability (determined by the trypan blue exclusion method; see **Materials and Methods** section for

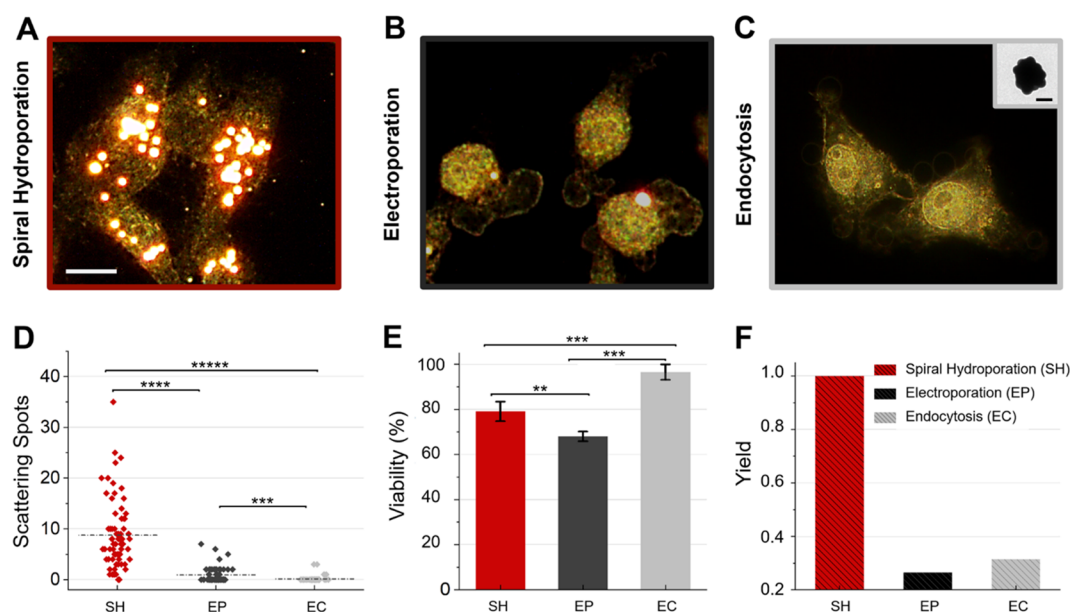


**Figure 5.** Intracellular delivery of GNPs (200 nm diameter). Dark-field scattering images verifying GNP delivery by (A) spiral hydroporation (SH), (B) electroporation (EP), and (C) endocytosis (EC) (scale bar: 20  $\mu\text{m}$ ). (Inset) TEM image of a GNP (scale bar: 100 nm). (D) Scattering spot counts, (E) cell viability, and (F) normalized yield for each method. All error bars represent the mean  $\pm 1$  SD ( $N = 3$ ); \*\*\* indicates a  $P$ -value below 0.001, \*\*\*\* indicates a  $P$ -value below 0.0001, and \*\*\*\*\* indicates a  $P$ -value below 0.00001.

details), at higher flow rates (*i.e.*, higher  $Re$ ), a minor decrease in viability could be observed (Figure 4D). This is to be expected, as cell perturbation is significantly greater at higher  $Re$ ; however, the difference in cell morphology and proliferation between spiral hydroporation and endocytosis was found to be negligible (Figure S4). To investigate cell viability further, *via* metabolic function, a standard MTT assay<sup>47</sup> was carried out (Materials and Methods section). Overall trends between trypan blue exclusion and MTT assays agreed well with each other, while MTT assays showed slightly lower viability values at high  $Re$  numbers (Figure 4D). Recently Liu *et al.*<sup>48</sup> reported that when cells were processed with mechanical deformation for intracellular delivery, they still maintained high nuclear envelope integrity and underwent low protein loss (*i.e.*, high cell membrane integrity). Since this work is also based on rapid cell deformation-enabled nanomaterial delivery, we consider that cells processed with our spiral hydroporator also preserve their nuclear and membrane integrity.

Next, we tested the effect of nanomaterial size on the delivery. Dextran having molecular weights in the range 3–2000 kDa, corresponding to a hydrodynamic diameter between 2–55 nm,<sup>49,50</sup> were used. Under the same flow conditions ( $Re = 366$ ), we calculated delivery efficiencies for five different FITC-dextran sizes (3–5, 70, 150, 500 and 2000 kDa) at the same concentration (see Materials and Methods for details). As shown in Figure 4E, delivery efficiency of at least 80% was achieved using our platform (see Figure S5 for MFI information). Relatively small dextrans (<70 kDa) were seen to have a higher delivery efficiency compared to larger ones (Figure 4E). For small dextrans, it is believed that both convective and diffusive transport of dextran across the cell membrane occurs, while convective transport dominates the transport of larger dextrans as suggested by Liu *et al.*<sup>24</sup> and Kizer *et al.*<sup>27</sup> We noticed that delivery efficiency remained at a similar level ( $\sim 82\%$ ), even as the dextran size increased from 150 to 2000 kDa. This trend suggested that there was potential

for larger molecules to be delivered, and in testing this concept, we were subsequently able to deliver 200 nm diameter GNPs (more details in the next section).

As discussed in the Design and Operating Principle section, the platform consists of a cross-junction and two T-junction channels (Figure 1), in which cells undergo sequential deformation–restoration processes. We hypothesized that this repeated deformation–restoration enhances delivery efficiency, and so to test this, a mixture of cells and 2000 kDa FITC-dextran was injected into (1) a channel with a cross-junction and (2) a channel with cross- and T-junctions, at  $Re = 366$ . The resultant delivery efficiencies have been plotted in Figure 4F (the results for other dextran sizes are plotted in Figure S5 and MFI information is presented in Figure S6). The figure shows that the sequential hydrodynamic cell perturbations exhibit a higher FITC-dextran delivery, which agreed well with results published for constriction-based intracellular delivery platforms, passing cells through bottle-necks in series.<sup>21,24</sup>

To compare our platform with the most popular intracellular delivery method, that is, electroporation, a Neon Transfection System (Thermo Fisher Scientific, Waltham, MA, USA) was employed. Note that we also prepared a plot (Figure S7) for detailed comparison between this work and other state-of-the-art microfluidic devices<sup>21,24–27,51</sup> tested under identical or similar concentrations. We delivered large (500 and 2000 kDa FITC-dextran) molecules into the same cell line, using two methods. For 2000 kDa FITC-dextran delivery, the spiral hydroporator exhibited approximately 4-fold higher delivery efficiency (Figure 4G; MFI values in Figure S8A) and showed  $\sim 13\%$  higher viability than the electroporator (Figure S8B). With regards to analyte consumption, based on the recipe recommended by the electroporator manufacturer, spiral hydroporation consumed approximately 2.5 times more than standard electroporation, per cell, when the same FITC-dextran concentration was used. This may be a potential drawback for spiral hydroporation, although adopting a

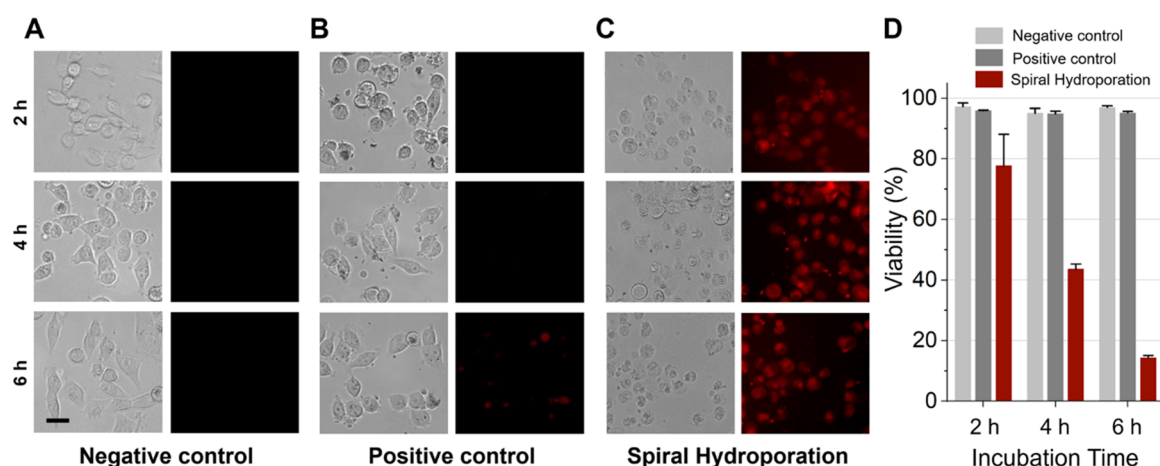


**Figure 6.** Intracellular delivery of MSNs. Bright-field and fluorescent images showing the cells during the delivery of doxorubicin-loaded MSNs for the (A) negative control, (B) positive control (cells coincubated with DOX-MSNs), and (C) spiral hydroporation (scale bar: 40  $\mu\text{m}$ ). (D) Time-dependent cell viability changes for (A–C). All error bars represent the mean  $\pm 1$  SD (N = 3).

pressure-driven flow control system<sup>36</sup> could be a simple solution, allowing significant sample volume (*i.e.*, mass) reduction.

**Intracellular Delivery of Gold Nanoparticles.** As briefly discussed, based on recent developments in the field of nanotechnology, a wide array of functional GNPs has been created, for numerous biological applications;<sup>52</sup> however, delivery to their biological targets at the subcellular level, with high efficiency and specificity, remains challenging. We hypothesized that our spiral hydroporator could be applied for GNP delivery, on the assumption that the vigorous spiral hydroporation process would facilitate delivery of large nanoparticles, such as GNPs, into cells.

To test this hypothesis, a series of GNP delivery experiments was performed. As shown in Figure 5A, extremely large GNPs (200 nm in diameter) were successfully delivered into MDA-MB-231 cells, *via* spiral hydroporation. To characterize this delivery, GNPs were imaged using dark-field microscopy (BX 43, Olympus, Tokyo, Japan); the scattering spots were counted and are shown in Figures 5D and S9. Note that not every scattering spot translates into a single GNP. It has been reported that nanoparticles tend to form clusters under cytosolic conditions, due to exposure to ions and protein,<sup>53,54</sup> so the scattering spots here indicate clustered GNPs in the cell, after delivery. An electroporator was also applied, to create a reference used in a performance comparison with hydroporation, and almost 10 times more scattering spots were observed for cells treated with the spiral hydroporation platform compared to those treated using the electroporator. The electroporator was able to deliver GNPs as well, although only a small number of scattering spots were detected (Figure 5B); this was to be expected, as it has been established that electroporation is not effective in transporting large nanomaterials (here GNPs), due to large counteracting effects of Stokes drag.

To confirm the GNP locations inside cells, a confocal microscope was employed for the imaging.<sup>55</sup> As presented in Figure S10 and Movie S8, most GNPs were seen in the cytosol, while some GNPs appeared in the nucleus region. This indicates that hydroporation may open the nucleus envelope, facilitating nucleus delivery, although further investigation into this concept is required.

We also investigated cell viability, and the results showed that the electroporator is more invasive to cells (Figure 5E). Regarding cell morphology (Figure 5A–C), cells treated with the spiral hydroporator were closer to the control endocytosis group, while those processed with the electroporator were rounder, implying that these cells underwent more stress.<sup>56</sup> We also calculated the normalized yield, by multiplying the scattering spot number by cell viability (Figure 5F), in a yield that can be used to directly compare overall performance. The results indicated that the spiral hydroporation platform is more than three times as effective, with respect to the GNP delivery.

#### Intracellular Delivery of Functional Nanoparticles.

We also investigated the possibility of using the spiral hydroporator to deliver functional nanoparticles. In this study, we chose 150 nm (diameter) mesoporous silica nanoparticles (MSNs), as popularly used for drug, protein, and nucleic acid nanocarriers. MSNs loaded with doxorubicin (DOX), an anticancer drug (the preparation steps in Materials and Methods section), were delivered to MDA-MB-231 cells using the spiral hydroporator, although other chemical choices can be made for various applications, depending on user needs.<sup>57</sup> At DOX-MSN delivery completion, the delivery amount was assessed, based on the intrinsic DOX fluorescence. As shown in Figure 6A–C, compared with endocytosis controls, cells treated with the spiral hydroporator showed much more intense fluorescence.

We also monitored morphological changes to the cells, testing the assumption that higher DOX delivery amounts led to faster cell death. After 2 h, cells treated with the spiral hydroporation platform were not polarized (*i.e.*, they showed a rounded shape), and morphological apoptosis features (Figure 6C at 6 h point) were observed. These morphological changes can be attributed to the fact that the DOX induces apoptosis,<sup>58</sup> leading to rapid cell death, and this was particularly clear for cells that had been processed with spiral hydroporation. DOX cytotoxicity to MDA-MB-231 cells was also determined using a trypan blue exclusion assay, as shown in Figure 6D, and after 6 h, approximately 85% of the cancer cells were found to be dead. Based on these results, we believe that our platform will be useful for investigating DOX-induced apoptosis, avoiding traditional surface ligands-based DOX delivery.

**Intracellular Delivery of mRNA.** Beyond nanoparticle delivery applications, we tested delivery of synthetic biomolecules, in this study, mRNAs. The mRNA (a basic, constitutively fluorescent, green fluorescent protein, EGFP, which is a 996-nucleotide mRNA construct) was chosen here for delivery into K562 cells to investigate the possibility of using the spiral hydroporation platform for chimeric antigen receptor-expressing T-cell (CAR-T), engineering-associated research. We assessed the EGFP protein expression, based on mRNA delivery (2  $\mu\text{g}/\text{mL}$ ), using a flow cytometer, and the results are presented in Figure 7A,B (see Figure S11 for MFI

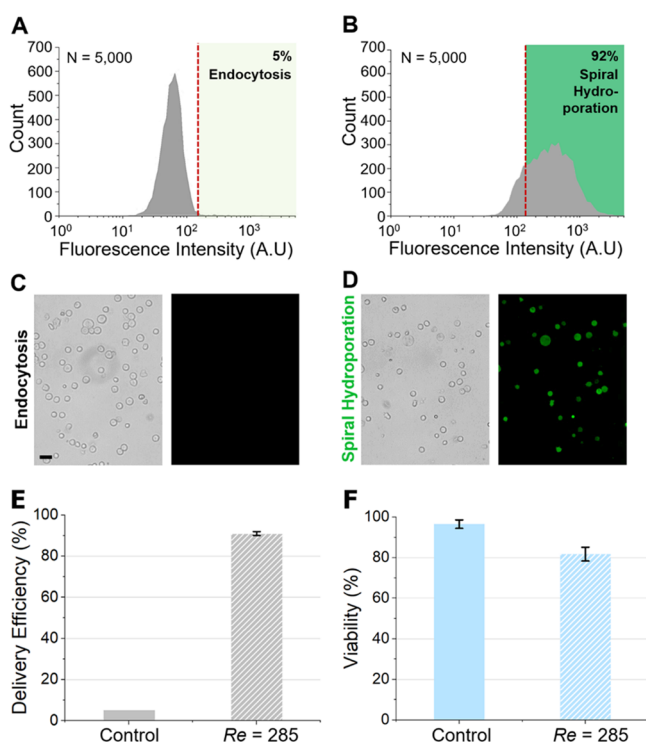


**Figure 7.** Intracellular delivery of mRNA. Fluorescence intensity histograms for: (A) endocytosis and (B) spiral hydroporation. Bright-field and fluorescent images showing delivery of the mRNA into K562 for EGFP expression *via* (C) endocytosis and (D) spiral hydroporation (scale bar: 40  $\mu\text{m}$ ). (E) Delivery efficiency and (F) cell viability results for cells treated with endocytosis and spiral hydroporation. All error bars represent the mean  $\pm 1$  SD ( $N = 3$ ).

information). After mRNA delivery, very strong EGFP signals were detected (Figure 7D), and a delivery efficiency of  $\sim 92\%$  was achieved, without sacrificing cell viability (Figure 7E,F), indicating our platform's high potential for use in immunotherapy research, although further investigation is required to test human immune cells.

## CONCLUSIONS

This work shows the use of intrinsic spiral cell deformation behavior originating from an instability-induced spiral vortex and vortex breakdown, in cross- and T-junction channels at moderate  $Re$ , for the intracellular delivery of nanomaterials. We have developed and validated a spiral hydroporation platform (a spiral hydroporator), which delivers various nanomaterials, including dextran, mRNA, GNP, and DOX-MSN. In contrast to other conventional delivery approaches, our method is characterized by a high efficiency, material/species-independency (including suspension cell lines) and robustness, while

achieving a low-cost, rapid, and simple operation. The platform does not require vectors, special buffers, or external instrumentation such as imaging microscopes, cameras, or voltage sources. Syringe pumps are the only technology required and are used to inject the cells mixed with the target nanomaterials into a PDMS microfluidic chip, demonstrating the high practicability and portability of the system. We compared our system with an existing, state-of-the-art tool, an electroporator, and other representative microfluidic platforms and were able to demonstrate superior performance. In conclusion, we envision that the spiral hydroporator will serve as an attractive intracellular nanomaterial delivery platform, influencing cell biology-associated research.

## MATERIALS AND METHODS

**Fabrication of Microfluidic Intracellular Device.** The microfluidic mold was fabricated using conventional photolithography, and polydimethylsiloxane (PDMS, Dow Corning Corporation, Corning, NY, USA) replicas were prepared using standard PDMS-molding protocols.

**Flow Simulation.** Flow through the cross-junction channel was simulated by the fluid dynamics software OpenFOAM.<sup>42</sup> The channel was numerically approximated using inlets and outlets at  $19D_h$  from the midpoint of the junction and 4  $\mu\text{m}$  chamfers at the corners of the constriction. A hexahedral mesh was generated by first constructing a uniform grid in the blockMesh utility and then using the snappyHexMesh function to incorporate the constricted section edge features. A no-slip boundary condition was applied to all walls. A uniform velocity was set for the inlets, and the pressure at the outlets was set to zero. Steady-state solutions were calculated using simpleFOAM, and transience was investigated using the icoFOAM solver. Both solvers have a residual tolerance of  $10^{-7}$  for velocity and pressure. A mesh convergence study was conducted at  $Re = 100$ , by iteratively refining the background grid and checking the relative error of the steady-state midpoint vorticity. Compared with a  $37.1 \times 10^6$  cell case, the relative error dropped to 2%, based on the use of  $8.4 \times 10^6$  cells, and to 1%, based on the use of  $16.0 \times 10^6$  cells (chosen as a suitable mesh).

**Flow Visualization.** 10  $\mu\text{M}$  Rhodamine 6G (Sigma-Aldrich, MO, USA) was added to DI water for flow visualization, and fluorescence was captured using a Zeiss Axio Observer A1 inverted microscope (Carl Zeiss, Oberkochen, Germany), equipped with an Andor Luca-R EMCCD camera (Oxford Instruments, Abingdon, UK).

**Cell Preparation.** MDA-MB-231 and K562 cells were cultured using standard protocols and resuspended in cell media with the target nanomaterial. For mRNA (Trilink Biotechnologies; CA, USA) delivery, Opti-MEM (Thermo Fisher Scientific, MA, USA) was used as a delivery buffer, for stabilization. 40  $\mu\text{m}$  cell strainers (Thermo Fisher Scientific, MA, USA) were used to filter dust from the cell suspensions before loading them into syringes. MDA-MB-231 and K562 cell lines were purchased from the Korean Cell Line Bank (Seoul, Republic of Korea).

**Cell Viability.** Cell viability was characterized by trypan blue exclusion assay (Lonza, MD, USA) and/or MTT assay (Thermo Fisher Scientific, MA, USA). Protocols recommended by the manufacturers were used for both assays. Triplicate sampling or more was conducted for each data point.

**FITC-Dextran Delivery.** All FITC-dextran materials (3–2000 kDa) were purchased from Sigma-Aldrich (MO, USA), and regardless of dextran sizes, every experiment was conducted using a concentration of 0.3 mg/mL delivery buffer (cell media). The mass of fluorophores in solution was identical across all molecules sizes.<sup>24</sup> For the endocytosis control group, cells were incubated with identical FITC-dextran during the spiral hydroporation process, and extra FITC-dextran were washed *via* centrifugation.

**Intracellular Delivery and Cell Motion Analysis Protocols.** Cell suspensions were injected using syringe pumps (Harvard Apparatus, MA, USA), with injection conducted only from the left-

hand side, to prevent two cells from simultaneously entering the deformation zone and affecting each other. Cell motions were recorded using a Phantom VEO710L high-speed camera (Vision Research, NJ, USA), with a frame rate between 250,000 and 680,000 frames/s and an exposure time ranging from 600 ns to 1  $\mu$ s. Images were processed using ImageJ (<https://imagej.nih.gov/ij/>). Normally, a concentration of  $5 \times 10^5$  cells/mL was used, and all fluorescence images were acquired 18 h after delivery, except for DOX-MSN images.

**Flow Cytometry.** Cell fluorescence was assessed using a flow cytometer (Guava easyCyte, EMD Millipore, MA, USA), a 488 nm laser for excitation, and a 533/30 nm emission filter for FITC and EGFP. Data analysis was carried out using Guava easyCyte software (guavaSoft 3.3).

**Electroporation Protocols.** Cells were processed with a Neon Transfection System (Thermo Fisher Scientific, MA, USA), using the specified buffer (Resuspension Buffer R) recommended by the manufacturer, depending on the cell type.

**Gold Nanoparticle Synthesis and Size Characterization.** Citrate-capped GNPs were synthesized in the laboratory using standard synthesis protocols,<sup>59,60</sup> and their sizes were characterized using an energy-filtering transmission electron microscope (LIBRA 120, Carl Zeiss, Oberkochen, Germany) and particle size analyzer (ELS-Z2, Otsuka Electronics, Osaka, Japan). All samples were analyzed in triplicate, and a GNP concentration of optical density (OD) of 0.02 was used.

**DOX-MSN Delivery.** Prior to delivery, DOX-MSN was prepared following procedures published in the literature.<sup>54,61</sup> Briefly, MSNs were fabricated with the sol-gel method, and the MSN suspension was mixed with DOX solution (500  $\mu$ g/mL), with an equivalent volume. In the last step, the MSN surface was modified with aminosilane, in aqueous solution, to prevent undesired leakages. After purification, the DOX-MSN was redispersed into the PBS as a stock. Cells with the diluted DOX-MSN (5  $\mu$ g/mL) were tested at  $Re = 346$ , and cell fluorescence was recorded for up to 6 h, using a Zeiss Axio Observer A1 inverted microscope (Carl Zeiss, Oberkochen, Germany).

## ASSOCIATED CONTENT

### Supporting Information

The Supporting Information is available free of charge at <https://pubs.acs.org/doi/10.1021/acsnano.9b07930>.

Figures S1–S11 (PDF)

Movie S1: Vortex-induced cell deformation at  $Re = 203$  (AVI)

Movie S2: Cell deformation in the cross-junction at  $Re = 285$  (AVI)

Movie S3: Cell deformation in the T-junction at  $Re = 285$  (AVI)

Movie S4: Numerical flow simulation in the cross-junction at  $Re = 122$  (static vortex core) (AVI)

Movie S5: Numerical flow simulation in the cross-junction at  $Re = 203$  (steady swirling flow) (AVI)

Movie S6: Numerical flow simulation in the cross-junction at  $Re = 285$  (periodic vortex breakup) (AVI)

Movie S7: Vortex breakdown-induced cell trapping and deformation at  $Re = 285$  (AVI)

Movie S8: Z-stack movie of an MDA-MB-231 cell, showing delivered GNP clusters (AVI)

## AUTHOR INFORMATION

### Corresponding Author

**Aram J. Chung** – Department of Bio-convergence Engineering, Department of Bioengineering, and School of Biomedical Engineering, Korea University, Seoul 02841, Republic of Korea; [orcid.org/0000-0003-4984-0222](https://orcid.org/0000-0003-4984-0222); Email: [ac467@korea.ac.kr](mailto:ac467@korea.ac.kr)

## Authors

**GeomYoung Kang** – Department of Bio-convergence Engineering, Korea University, Seoul 02841, Republic of Korea; [orcid.org/0000-0002-3660-0281](https://orcid.org/0000-0002-3660-0281)

**Daniel W. Carlson** – Micro/Bio/Nanofluidics Unit, Okinawa Institute of Science and Technology Graduate University (OIST), Okinawa 904-0495, Japan; [orcid.org/0000-0002-0171-1934](https://orcid.org/0000-0002-0171-1934)

**Tae Ho Kang** – Department of Life Science, University of Seoul, Seoul 02504, Republic of Korea

**Seungki Lee** – Department of Life Science, University of Seoul, Seoul 02504, Republic of Korea

**Simon J. Haward** – Micro/Bio/Nanofluidics Unit, Okinawa Institute of Science and Technology Graduate University (OIST), Okinawa 904-0495, Japan; [orcid.org/0000-0002-1884-4100](https://orcid.org/0000-0002-1884-4100)

**Inhee Choi** – Department of Life Science, University of Seoul, Seoul 02504, Republic of Korea; [orcid.org/0000-0002-1996-2926](https://orcid.org/0000-0002-1996-2926)

**Amy Q. Shen** – Micro/Bio/Nanofluidics Unit, Okinawa Institute of Science and Technology Graduate University (OIST), Okinawa 904-0495, Japan; [orcid.org/0000-0002-1222-6264](https://orcid.org/0000-0002-1222-6264)

Complete contact information is available at: <https://pubs.acs.org/10.1021/acsnano.9b07930>

## Notes

The authors declare no competing financial interest.

## ACKNOWLEDGMENTS

A.C. acknowledges the Samsung Research Funding and Incubation Center for Future Technology (grant no. SRFC-IT1802-03) to conduct all experimental studies. S.H. and A.S. gratefully acknowledge the Okinawa Institute of Science and Technology Graduate University, and financial support from the Cabinet Office, Government of Japan, and funding from the Japan Society for the Promotion of Science (grant nos. 17K06173, 18K03958, and 18H01135) with computational resources provided by the Scientific Computing section of Research Support Division at OIST for numerical studies. The authors would like to thank Prof. Ssang-Goo Cho at Konkuk University, Prof. Jae-Yong Park and Yeonju Bae at Korea University, Hyun Ji An at the University of Seoul, and all members of the Biomicrofluidics Laboratory at Korea University for their technical support and useful discussions. Provisional patents have been filed by the authors' institutions.

## REFERENCES

- (1) Chou, L. Y. T.; Ming, K.; Chan, W. C. W. Strategies for the Intracellular Delivery of Nanoparticles. *Chem. Soc. Rev.* **2011**, *40*, 233–245.
- (2) Cai, W.; Chen, X. Nanoplatfoms for Targeted Molecular Imaging in Living Subjects. *Small* **2007**, *3*, 1840–1854.
- (3) Duncan, B.; Kim, C.; Rotello, V. M. Gold Nanoparticle Platforms as Drug and Biomacromolecule Delivery Systems. *J. Controlled Release* **2010**, *148*, 122–127.
- (4) Ghosh, P.; Han, G.; De, M.; Kim, C. K.; Rotello, V. M. Gold Nanoparticles in Delivery Applications. *Adv. Drug Delivery Rev.* **2008**, *60*, 1307–1315.
- (5) Buck, J.; Grossen, P.; Cullis, P. R.; Huwyler, J. R.; Witzigmann, D. Lipid-Based DNA Therapeutics: Hallmarks of Non-Viral Gene Delivery. *ACS Nano* **2019**, *13*, 3754–3782.
- (6) Castanotto, D.; Rossi, J. J. The Promises and Pitfalls of RNA-Interference-Based Therapeutics. *Nature* **2009**, *457*, 426–433.
- (7) Transmembrane Transport of Ions and Small Molecules. In *Molecular Cell Biology*; Kaiser, C. A., Krieger, M., Lodish, H., Berk, A., Ed.; W.H. Freeman and Company: New York, 2007; pp 437–475.

- (8) Yoo, J.-W.; Irvine, D. J.; Discher, D. E.; Mitragotri, S. Bio-Inspired, Bioengineered and Biomimetic Drug Delivery Carriers. *Nat. Rev. Drug Discovery* **2011**, *10*, 521–535.
- (9) Sahay, G.; Querbes, W.; Alabi, C.; Eltoukhy, A.; Sarkar, S.; Zurenko, C.; Karagiannis, E.; Love, K.; Chen, D.; Zoncu, R.; Buganim, Y.; Schroeder, A.; Langer, R.; Anderson, D. G. Efficiency of siRNA Delivery by Lipid Nanoparticles is Limited by Endocytic Recycling. *Nat. Biotechnol.* **2013**, *31*, 653–658.
- (10) Stewart, M. P.; Sharei, A.; Ding, X.; Sahay, G.; Langer, R.; Jensen, K. F. *In Vitro* and *Ex Vivo* Strategies for Intracellular Delivery. *Nature* **2016**, *538*, 183–192.
- (11) Wu, Y.-C.; Wu, T.-H.; Clemens, D. L.; Lee, B.-Y.; Wen, X.; Horwitz, M. A.; Teitell, M. A.; Chiou, P.-Y. Massively Parallel Delivery of Large Cargo into Mammalian Cells with Light Pulses. *Nat. Methods* **2015**, *12*, 439–444.
- (12) Xu, X.; Hou, S.; Wattanatorn, N.; Wang, F.; Yang, Q.; Zhao, C.; Yu, X.; Tseng, H.-R.; Jonas, S. J.; Weiss, P. S. Precision-Guided Nanospers for Targeted and High-Throughput Intracellular Gene Delivery. *ACS Nano* **2018**, *12*, 4503–4511.
- (13) Cao, Y.; Chen, H.; Qiu, R.; Hanna, M.; Ma, E.; Hjort, M.; Zhang, A.; Lewis, R. S.; Wu, J. C.; Melosh, N. A. Universal Intracellular Biomolecule Delivery with Precise Dosage Control. *Sci. Adv.* **2018**, *4*, No. eaat8131.
- (14) Saklayen, N.; Huber, M.; Madrid, M.; Nuzzo, V.; Vulis, D. I.; Shen, W.; Nelson, J.; McClelland, A. A.; Heisterkamp, A.; Mazur, E. Intracellular Delivery Using Nanosecond-Laser Excitation of Large-Area Plasmonic Substrates. *ACS Nano* **2017**, *11*, 3671–3680.
- (15) Man, T.; Zhu, X.; Chow, Y. T.; Dawson, E. R.; Wen, X.; Patananan, A. N.; Liu, T. L.; Zhao, C.; Wu, C.; Hong, J. S.; Chung, P.-S.; Clemens, D. L.; Lee, B.-Y.; Weiss, P. S.; Teitell, M. A.; Chiou, P.-Y. Intracellular Photothermal Delivery for Suspension Cells Using Sharp Nanoscale Tips in Microwells. *ACS Nano* **2019**, *13*, 10835–10844.
- (16) Huang, J.-A.; Caprettini, V.; Zhao, Y.; Melle, G.; Maccaferri, N.; Deleje, L.; Zambrana-Puyalto, X.; Ardini, M.; Tantussi, F.; Dipalo, M.; De Angelis, F. On-Demand Intracellular Delivery of Single Particles in Single Cells by 3D Hollow Nanoelectrodes. *Nano Lett.* **2019**, *19*, 722–731.
- (17) Wang, Y.; Yang, Y.; Yan, L.; Kwok, S. Y.; Li, W.; Wang, Z.; Zhu, X.; Zhu, G.; Zhang, W.; Chen, X.; Shi, P. Poking Cells for Efficient Vector-Free Intracellular Delivery. *Nat. Commun.* **2014**, *5*, 4466.
- (18) Cao, Y.; Ma, E.; Cestellos-Blanco, S.; Zhang, B.; Qiu, R.; Su, Y.; Doudna, J. A.; Yang, P. Nontoxic Nanopore Electroporation for Effective Intracellular Delivery of Biological Macromolecules. *Proc. Natl. Acad. Sci. U. S. A.* **2019**, *116*, 7899–7904.
- (19) Shalek, A. K.; Robinson, J. T.; Karp, E. S.; Lee, J. S.; Ahn, D.-R.; Yoon, M.-H.; Sutton, A.; Jorgolli, M.; Gertner, R. S.; Gujral, T. S.; MacBeath, G.; Yang, E. G.; Park, H. Vertical Silicon Nanowires as a Universal Platform for Delivering Biomolecules into Living Cells. *Proc. Natl. Acad. Sci. U. S. A.* **2010**, *107*, 1870–1875.
- (20) Sonnen, K. F.; Merten, C. A. Microfluidics as an Emerging Precision Tool in Developmental Biology. *Dev. Cell* **2019**, *48*, 293–311.
- (21) Sharei, A.; Zoldan, J.; Adamo, A.; Sim, W. Y.; Cho, N.; Jackson, E.; Mao, S.; Schneider, S.; Han, M. J.; Lytton-Jean, A.; Basto, P. A.; Jhunjhunwala, S.; Lee, J.; Heller, D. A.; Kang, J. W.; Hartoularos, G. C.; Kim, K. S.; Anderson, D. G.; Langer, R.; Jensen, K. F. A Vector-Free Microfluidic Platform for Intracellular Delivery. *Proc. Natl. Acad. Sci. U. S. A.* **2013**, *110*, 2082–2087.
- (22) Han, X.; Liu, Z.; Jo, M. C.; Zhang, K.; Li, Y.; Zeng, Z.; Li, N.; Zu, Y.; Qin, L. CRISPR-Cas9 Delivery to Hard-To-Transfect Cells via Membrane Deformation. *Sci. Adv.* **2015**, *1*, No. e1500454.
- (23) Jarrell, J. A.; Twite, A. A.; Lau, K. H. W. J.; Kashani, M. N.; Lievano, A. A.; Acevedo, J.; Priest, C.; Nieva, J.; Gottlieb, D.; Pawell, R. S. Intracellular Delivery of mRNA to Human Primary T Cells with Microfluidic Vortex Shedding. *Sci. Rep.* **2019**, *9*, 3214.
- (24) Liu, A.; Islam, M.; Stone, N.; Varadarajan, V.; Jeong, J.; Bowie, S.; Qiu, P.; Waller, E. K.; Alexeev, A.; Sulchek, T. Microfluidic Generation of Transient Cell Volume Exchange for Convectively Driven Intracellular Delivery of Large Macromolecules. *Mater. Today* **2018**, *21*, 703–712.
- (25) Deng, Y.; Kizer, M.; Rada, M.; Sage, J.; Wang, X.; Cheon, D.-J.; Chung, A. J. Intracellular Delivery of Nanomaterials via an Inertial Microfluidic Cell Hydroperator. *Nano Lett.* **2018**, *18*, 2705–2710.
- (26) Xing, X.; Pan, Y.; Yobas, L. A Low-Backpressure Single-Cell Point Constriction for Cytosolic Delivery Based on Rapid Membrane Deformations. *Anal. Chem.* **2018**, *90*, 1836–1844.
- (27) Kizer, M. E.; Deng, Y.; Kang, G.; Mikael, P. E.; Wang, X.; Chung, A. J. Hydroperator: A Hydrodynamic Cell Membrane Perforator for High-Throughput Vector-Free Nanomaterial Intracellular Delivery and DNA Origami Biostability Evaluation. *Lab Chip* **2019**, *19*, 1747–1754.
- (28) Gossett, D. R.; Tse, H. T. K.; Lee, S. A.; Ying, Y.; Lindgren, A. G.; Yang, O. O.; Rao, J.; Clark, A. T.; Di Carlo, D. Hydrodynamic Stretching of Single Cells for Large Population Mechanical Phenotyping. *Proc. Natl. Acad. Sci. U. S. A.* **2012**, *109*, 7630–7635.
- (29) Perkins, T. T.; Smith, D. E.; Chu, S. Single Polymer Dynamics in an Elongational Flow. *Science* **1997**, *276*, 2016–2021.
- (30) Kalashnikov, V. N.; Tsiklauri, M. G. Effect of Polymer Additives on Ordered Three-Dimensional Structures Arising in Cross-Slot Flow. *J. Non-Newtonian Fluid Mech.* **1993**, *48*, 215–223.
- (31) Haward, S. J.; Poole, R. J.; Alves, M. A.; Oliveira, P. J.; Goldenfeld, N.; Shen, A. Q. Tricritical Spiral Vortex Instability in Cross-Slot Flow. *Phys. Rev. E: Stat. Phys., Plasmas, Fluids, Relat. Interdiscip. Top.* **2016**, *93*, No. 031101.
- (32) Burshtein, N.; Zografos, K.; Shen, A. Q.; Poole, R. J.; Haward, S. J. Inertioelastic Flow Instability at a Stagnation Point. *Phys. Rev. X* **2017**, *7*, No. 041039.
- (33) Chung, A. J. A Minireview on Inertial Microfluidics Fundamentals: Inertial Particle Focusing and Secondary Flow. *BioChip J.* **2019**, *13*, 53–63.
- (34) Chung, A. J.; Gossett, D. R.; Di Carlo, D. Three Dimensional, Sheathless, and High-Throughput Microparticle Inertial Focusing through Geometry-Induced Secondary Flows. *Small* **2013**, *9*, 685–690.
- (35) Kim, G. Y.; Han, J. I.; Park, J. K. Inertial Microfluidics-Based Cell Sorting. *BioChip J.* **2018**, *12*, 257–267.
- (36) Deng, Y.; Davis, S. P.; Yang, F.; Paulsen, K. S.; Kumar, M.; Sinnott DeVaux, R.; Wang, X.; Conklin, D. S.; Oberai, A.; Herschkowitz, J. I.; Chung, A. J. Inertial Microfluidic Cell Stretcher (iMCS): Fully Automated, High-Throughput, and Near Real-Time Cell Mechanotyping. *Small* **2017**, *13*, 1700705.
- (37) Sharei, A.; Poceviciute, R.; Jackson, E. L.; Cho, N.; Mao, S.; Hartoularos, G. C.; Jang, D. Y.; Jhunjhunwala, S.; Eyerman, A.; Schoettle, T.; Langer, R.; Jensen, K. F. Plasma Membrane Recovery Kinetics of a Microfluidic Intracellular Delivery Platform. *Integr. Biol.* **2014**, *6*, 470–475.
- (38) Tse, H. T. K.; Gossett, D. R.; Moon, Y. S.; Masaeli, M.; Sohsmann, M.; Ying, Y.; Mislick, K.; Adams, R. P.; Rao, J.; Di Carlo, D. Quantitative Diagnosis of Malignant Pleural Effusions by Single-Cell Mechanophenotyping. *Sci. Transl. Med.* **2013**, *5*, 212ra163.
- (39) Lin, J.; Kim, D.; Tse, H. T.; Tseng, P.; Peng, L.; Dhar, M.; Karumbayaram, S.; Di Carlo, D. High-Throughput Physical Phenotyping of Cell Differentiation. *Microsyst. Nanoeng.* **2017**, *3*, 17013.
- (40) Zhang, J.-W.; Li, W.-F.; Xu, X.-L.; Liu, H.-F.; Wang, F.-C. Experimental Investigation of Three-Dimensional Flow Regimes in a Cross-Shaped Reactor. *Phys. Fluids* **2019**, *31*, No. 034105.
- (41) Zhang, J.-W.; Yao, T. I.; Li, W. F.; El Hassan, M.; Xu, X. I.; Liu, H. F.; Wang, F. C. Trapping Region of Impinging Jets in a Cross-Shaped Channel. *AIChE J.* **2020**, *66*, No. e16822.
- (42) Weller, H. G.; Tabor, G.; Jasak, H.; Fureby, C. A Tensorial Approach to Computational Continuum Mechanics Using Object-Oriented Techniques. *Comput. Phys.* **1998**, *12*, 620–631.
- (43) Vigolo, D.; Radl, S.; Stone, H. A. Unexpected Trapping of Particles at a T Junction. *Proc. Natl. Acad. Sci. U. S. A.* **2014**, *111*, 4770–4775.

- (44) Chan, S. T.; Haward, S. J.; Shen, A. Q. Microscopic Investigation of Vortex Breakdown in a Dividing T-Junction Flow. *Phys. Rev. Fluids* **2018**, *3*, No. 072201.
- (45) Lucca-Negro, O.; O'doherty, T. Vortex Breakdown: A Review. *Prog. Energy Combust. Sci.* **2001**, *27*, 431–481.
- (46) Sharma, V.; Park, K.; Srinivasarao, M. Shape Separation of Gold Nanorods Using Centrifugation. *Proc. Natl. Acad. Sci. U. S. A.* **2009**, *106*, 4981–4985.
- (47) Van Meerloo, J.; Kaspers, G. J. L.; Cloos, J. Cell Sensitivity Assays: The MTT Assay. In *Cancer Cell Culture*; Cree, I. A., Ed.; Springer: New York, 2011; pp237–245.
- (48) Liu, A.; Yu, T.; Young, K.; Stone, N.; Hanasoge, S.; Kirby, T. J.; Varadarajan, V.; Colonna, N.; Liu, J.; Raj, A.; Lammerding, J.; Alexeev, A.; Sulchek, T. Cell Mechanical and Physiological Behavior in the Regime of Rapid Mechanical Compressions that Lead to Cell Volume Change. *Small* **2020**, *16*, No. 1903857.
- (49) Choi, J. J.; Wang, S.; Tung, Y.-S.; Morrison, B., III; Konofagou, E. E. Molecules of Various Pharmacologically-Relevant Sizes Can Cross the Ultrasound-Induced Blood-Brain Barrier Opening *In Vivo*. *Ultrasound Med. Biol.* **2010**, *36*, 58–67.
- (50) Lebrun, L.; Junter, G.-A. Diffusion of Dextran through Microporous Membrane Filters. *J. Membr. Sci.* **1994**, *88*, 253–261.
- (51) Hallow, D. M.; Seeger, R. A.; Kamaev, P. P.; Prado, G. R.; LaPlaca, M. C.; Prausnitz, M. R. Shear-Induced Intracellular Loading of Cells with Molecules by Controlled Microfluidics. *Biotechnol. Bioeng.* **2008**, *99*, 846–854.
- (52) Pissuwan, D.; Niidome, T.; Cortie, M. B. The Forthcoming Applications of Gold Nanoparticles in Drug and Gene Delivery Systems. *J. Controlled Release* **2011**, *149*, 65–71.
- (53) Lacerda, S. H. D. P.; Park, J. J.; Meuse, C.; Pristiniski, D.; Becker, M. L.; Karim, A.; Douglas, J. F. Interaction of Gold Nanoparticles with Common Human Blood Proteins. *ACS Nano* **2010**, *4*, 365–379.
- (54) Albanese, A.; Chan, W. C. W. Effect of Gold Nanoparticle Aggregation on Cell Uptake and Toxicity. *ACS Nano* **2011**, *5*, 5478–5489.
- (55) Klein, S.; Petersen, S.; Taylor, U.; Rath, D.; Barcikowski, S. Quantitative Visualization of Colloidal and Intracellular Gold Nanoparticles by Confocal Microscopy. *J. Biomed. Opt.* **2010**, *15*, No. 036015.
- (56) Joshi, R. P.; Schoenbach, K. H. Mechanism for Membrane Electroporation Irreversibility under High-Intensity, Ultrashort Electrical Pulse Conditions. *Phys. Rev. E: Stat. Phys., Plasmas, Fluids, Relat. Interdiscip. Top.* **2002**, *66*, No. 052901.
- (57) Wu, K. C.-W.; Yamauchi, Y. Controlling Physical Features of Mesoporous Silica Nanoparticles (MSNs) for Emerging Applications. *J. Mater. Chem.* **2012**, *22*, 1251–1256.
- (58) Kalyanaraman, B.; Joseph, J.; Kalivendi, S.; Wang, S.; Konorev, E.; Kotamraju, S. Doxorubicin-Induced Apoptosis: Implications in Cardiotoxicity. *Mol. Cell. Biochem.* **2002**, *234*, 119–124.
- (59) Aslan, K.; Pérez-Luna, V. H. Surface Modification of Colloidal Gold by Chemisorption of Alkanethiols in the Presence of a Nonionic Surfactant. *Langmuir* **2002**, *18*, 6059–6065.
- (60) Li, J.; Wu, J.; Zhang, X.; Liu, Y.; Zhou, D.; Sun, H.; Zhang, H.; Yang, B. Controllable Synthesis of Stable Urchin-Like Gold Nanoparticles Using Hydroquinone to Tune the Reactivity of Gold Chloride. *J. Phys. Chem. C* **2011**, *115*, 3630–3637.
- (61) Lee, S.; Kwon, J. A.; Park, K. H.; Jin, C. M.; Joo, J. B.; Choi, I. Controlled Drug Release with Surface-Capped Mesoporous Silica Nanoparticles and Its Label-Free *In Situ* Raman Monitoring. *Eur. J. Pharm. Biopharm.* **2018**, *131*, 232–239.